Applied Energy 196 (2017) 82–96

Contents lists available at ScienceDirect

Applied Energy

journal homepage: www.elsevier.com/locate/apenergy

Experimental study of wake structure behind a horizontal axis tidal stream turbine

Yaling Chen [a], Binliang Lin [a,*], Jie Lin [a], Shujie Wang [b]

[a] State Key Laboratory of Hydro-science and Engineering, Tsinghua University, Beijing 100084, China
[b] College of Engineering, Ocean University of China, Qingdao, Shandong 266100, China

HIGHLIGHTS

- Full wake structure of a horizontal axis turbine is experimentally studied.
- With a low TSR, the maximum velocity deficit occurs at the wake core.
- Wake rotation is non-uniform, which impacts on the process of wake mixing.
- Wake turbulence is strong and anisotropic and spreads largely in transverse direction.
- Near-wake is influenced by turbine stanchion, especially along water depth.

ARTICLE INFO

Article history:
Received 16 December 2016
Received in revised form 11 March 2017
Accepted 31 March 2017
Available online 6 April 2017

Keywords:
Tidal stream turbine
Wake velocity deficit
Wake rotation
Turbulence intensity
Turbulence anisotropy

ABSTRACT

A detailed experimental investigation of the wake propagation behind a horizontal axis turbine with three blades was conducted in a recirculating water flume. An Acoustic Doppler Velocimeter was employed to measure the time varying velocities at fifteen depths across the width of the open flume to obtain the three-dimensional velocity and turbulence fields within the length of 20 Rotor Diameters downstream. The experimental results indicated that velocity reduction in the wake was caused by both the kinetic energy extraction and blockage effects of the tidal stream turbine rotor and stanchion. The maximum velocity deficit occurred at the wake core due to a lower tip speed ratio and blockage of the hub. The wake strip gradually enlarged with the distance downstream, with less mixing in the transverse direction. The wake zone shifted towards the water surface in the vertical direction, which mainly resulted from the merging of two wakes induced by turbine rotor and stanchion. The wake rotation was also observed, and the maximum circumfluence velocity was approximately 20% of the streamwise velocity; thus, it had a significant influence on the process of near wake mixing. Furthermore, the wake turbulence of the turbine was strong and anisotropic, which would have an impact on the behaviour of other turbines located downstream if they were in a turbine array. In addition, the turbine stanchion had a visible influence on the wake structure, especially near the wake, which should not be neglected when studying the wake characteristics.

1. Introduction

Marine renewable energy is expected to be increasingly harnessed because the ocean covers two thirds of the earth surface and has abundant energy resources. With the advantage of predictability, tidal current energy has shown great potential to be used for generating electricity in coastal waters [1–3]. Various tidal stream turbines have been designed to convert the kinetic energy of tidal currents into electrical power [4–6]. However, the power capacity of a tidal stream turbine is limited by the classic Lanchester-Betz theory [7]. Multiple tidal turbines should be combined to form an array to maximize the extractable power at a given site [8–11].

To determine the optimal layout of a turbine array, several studies have been undertaken to investigate the effects of array scale [12,13] as well as configuration [14,15] on the power output. Also, energy extraction by a turbine induces a wake flow, which may disturb the currents passing through the turbines downstream and impact on their performance [16–18]. Thus, it is crucial to understand the turbine wake evolution process and the interactions between turbine wakes [19,20].

* Corresponding author.
E-mail address: linbl@mail.tsinghua.edu.cn (B. Lin).

http://dx.doi.org/10.1016/j.apenergy.2017.03.126
0306-2619/

Computational fluid dynamics (CFD) codes have been widely employed to investigate the wake structure of tidal current turbines [21,22]. Sun et al. [23] used a CFD code to predict local-flow changes resulting from the tidal current energy extraction. A substantial drop in the free surface level was observed in the wake immediately behind the turbine rotor. Mason-Jones et al. [24] showed that the presence of a turbine stanchion resulted in an asymmetric wake downstream, but did not provide much detail about the wake velocity profiles. Lam and Chen [25], Lam et al. [26] proposed a recovery equation to determine the minimum wake velocity along the rotation axis downstream, and predicted the lateral velocity distribution based on Gaussian probability distribution. Brutto et al. [27] expressed the radius expansion of a far wake as a function of the ambient turbulence and thrust coefficient to simulate the wake evolution of an isolated turbine. Regarding turbine rotation, Shives and Crawford [28] adapted the actuator disc-RANS simulation by including the k-ω SST turbulence model to predict the wake turbulence resulting from the breakdown of trailed vortices from blade tips. Morris et al. [29] showed the swirl characteristics of a turbine wake and pointed out that the wake swirl was slightly affected by the blade number of turbine rotor in the near wake. To reveal the evolution process of turbine wakes, it is still necessary to validate the wake characteristics predicted by CFD simulations. However, observations of turbine wakes in natural waters are not available yet.

Myers and Bahaj [30], Myers and Bahaj [31] used an actuator disc to analyse the principal parameters that govern the development of a wake structure behind a horizontal axis turbine. The recovery rate of the wake structure was affected by the ambient flow turbulence. Harrison et al. [32] and Nguyen et al. [33] compared the RANS model results to experimental data measured behind a disc. It was found that the wake velocity and turbulence intensity were well simulated in the far wake, while wake turbulence intensity was underestimated in the vicinity of the disc. Batten et al. [34] also compared the results of numerical model with experimental data, and similar results were obtained. The wake rotation behind a turbine rotor cannot be shown by the experiments using an actuator disc.

Further experimental studies were undertaken to investigate wake propagation using scaled model turbines [35–37]. Stallard et al. [38] measured flow velocities along axes behind a horizontal axis turbine rotor, with Tip Speed Ratio (TSR) being about 4.7, to investigate the wake recovery. The maximum velocity deficit occurred around the rotation axis, but the high turbulence intensity occurred at blade tips in the near wake. Mycek et al. [39], Mycek et al. [40] showed the distribution of the velocity deficit and wake turbulence at a horizontal plane across turbine centre within 10 RD downstream. It was found that the wake shape and length were considerably influenced by the ambient turbulence intensity. Tedds et al. [41] carried out experiments using a model turbine with TSR being 6.15. The largest velocity deficit occurred at the blade tips, and the near wake turbulence was strongly anisotropic due to swirl effects. With detailed velocity measurements, Stallard et al. [42] showed the development characteristics of wake rotation and vorticity within 2 RD behind the turbine rotor. Atcheson et al. [43] conducted towing tests in a lake using a 1:10th scale horizontal axis turbine and measured the velocities along the turbine axis within 5 RD downstream. The varying inflow velocity induced little difference in wake velocity deficit, but it had a marked influence on the wake turbulence intensity. Indeed, the characteristics of turbine wake induced by the towing test were different from that produced by open channel flows. Morandi et al. [19] measured the flow velocities at 0.125 RD behind a scaled model turbine to investigate the influence of TSR on the three-dimensional velocity deficit and wake turbulence immediately downstream.

It can be seen from the existing studies that the effects of tidal current energy extraction on wake development have been investigated using both the CFD models and experiments in open channel flows. However, the three-dimensional characteristics of the wake structure still lack a good understanding. The experimental data measured behind scaled model turbine were largely limited to the axes of turbine rotors or a few cross-sections in the near wake, the whole evolution process of the three-dimensional structure of turbine wake was hardly revealed due to lack of the measured data. However, the performance of a tidal stream turbine located in a large array is influenced primarily by wake structure, especially in the far wake, of the upstream turbine. A good understanding of the evolution process of the wake structure is crucial to optimize the arrangement of tidal turbine array in the next stage.

In the current study, experiments were conducted in an open flume to further investigate wake structure of a horizontal axis turbine with three blades. The three-dimensional velocities were measured at sixteen cross-sections from 1 RD upstream to 20 RD downstream of the turbine to analyse the development of wake velocity deficit, wake rotation and wake turbulence. The aim of the study was to enhance our understanding of the whole wake evolution process and its three-dimensional characteristics. Furthermore, the experimental results could provide measured data for validating the results from numerical model simulations conducted to investigate the influence of horizontal axis turbines on the tidal flow and turbulence fields.

2. Experimental set-up

The experiment was conducted in a re-circulating water flume using a horizontal axis tidal stream turbine with three blades. The three-dimensional velocities were measured at sixteen cross-sections to investigate the wake characteristics behind the turbine in the flume. All of the measurements were obtained based on the same turbine operating and inflow conditions.

2.1. Flume configuration

Tests were undertaken in a model channel located within a re-circulating water flume, and the channel bed and walls were made of perspex panels. The testing section of the rectangular flume was 14.4 m long by 0.8 m wide and 0.8 m deep, and the water depth was 0.54 m. A 4.0 m long transition section was used to generate a smooth connection to the test section and to increase the flow velocity, as well as to steady the flow pattern. As shown in Fig. 1, a vertical porous plate with rectangular grids was fitted at the flume inlet to remove large scale eddies from the tank underneath the flume. This resulted in a spatially, nearly uniform velocity distribution and anisotropic turbulence at the inlet of the flume. The form of the transition section in x-y plane along the flow direction follows a hyperbolic relationship:

$$y = \pm 0.2\sqrt{16 - 3x_0} \tag{1}$$

where x_0 in the flow direction is $0m \leqslant x_0 \leqslant 4m$, with the width varying from 1.6 m to 0.8 m. Between the testing section and water outlet, there was another section that was 2 m long by 1.6 m wide. A similar porous plate was located at the outlet to reduce water level oscillations downstream.

The flow velocity field employed the right-handed coordinate system, with the turbine rotor centre as the coordinate origin O (0, 0, 0), as shown in Fig. 2a. The longitudinal, transverse and vertical axes are denoted as x, y and z, respectively. Correspondingly, the longitudinal, transverse and vertical velocities are denoted as u, v and w, respectively.

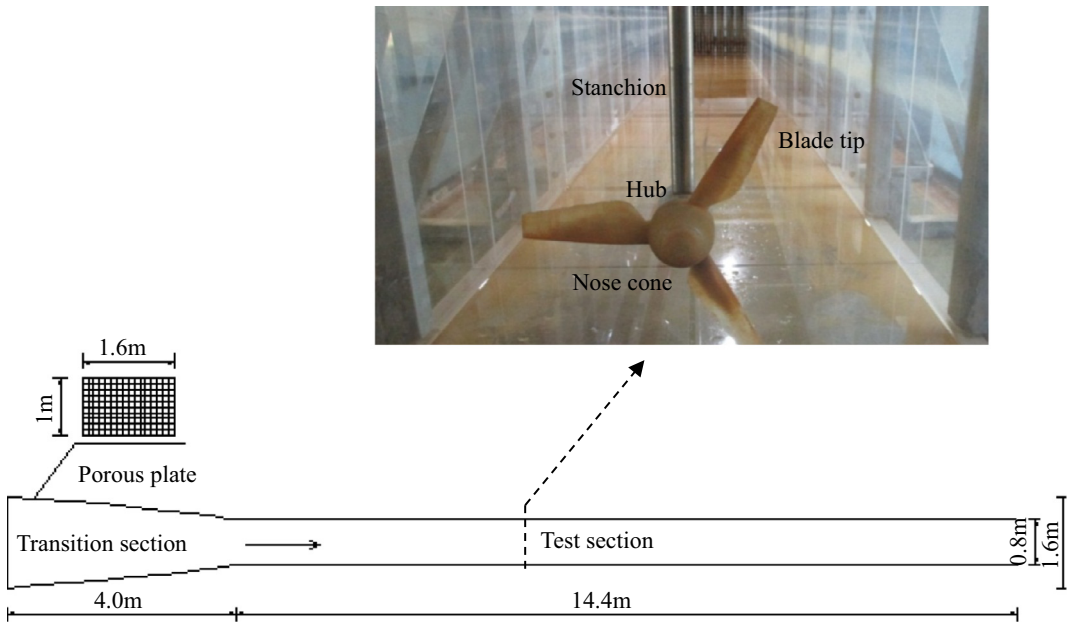

Fig. 1. Schematic of the hydraulic re-circulating water flume and the location of the three blades turbine.

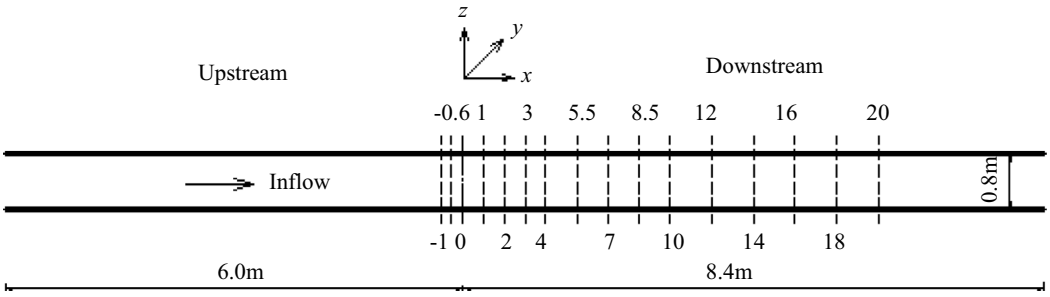

(a) Locations of cross-sections where velocity measurement was made, the numbers on both sides of dash lines denote the distance (RD) from turbine rotor plane.

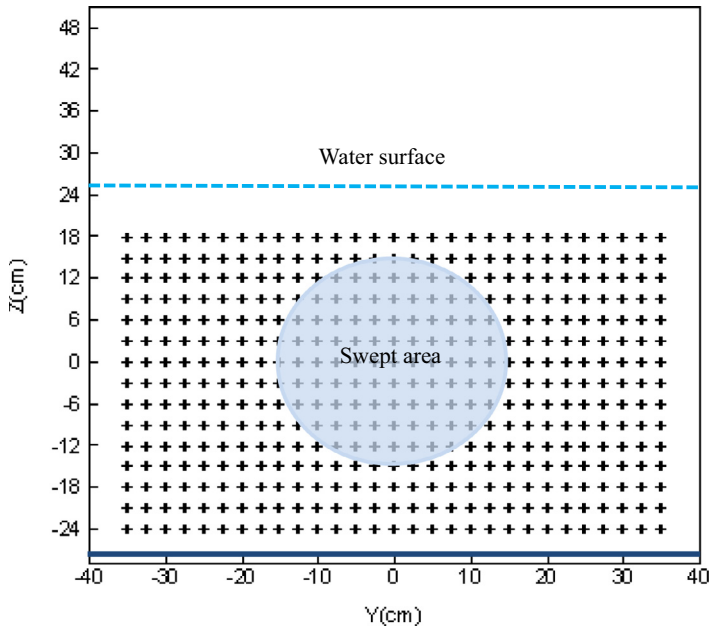

(b) Locations of velocity measurement made at all cross-sections except the blade swept area.

Fig. 2. Velocity measurement locations.

2.2. Model turbine

A three-bladed turbine rotor was employed to extract kinetic energy from the flow passing through the rotor swept area. The rotor diameter was 0.3 m, and the pitch angle was 15°. A description of blade profile is given in Table 1. As seen in Fig. 1, the turbine rotor was mounted on the centreline of the channel by a stanchion, and the hub height of the turbine rotor was 0.29 m above the floor. In the vertical direction, the top of the turbine rotor tip was submerged 0.1 m below the water surface and the bottom of the rotor tip was 0.14 m above the floor. In the longitudinal direction, the rotor was located 10.0 m from the flume inlet and 10.4 m from the flume outlet.

The hydrodynamic performance of the tidal stream turbine is usually represented by several parameters, including the blockage ratio, TSR, thrust coefficient and power coefficient.

The blockage ratio α is defined as the ratio of the rotor swept area $A_t = \pi R^2$ to the cross-section area of flow $A = LH$:

$$\alpha = \frac{A_t}{A} = \frac{\pi R^2}{LH} \tag{2}$$

where R = 0.15 m is the rotor radius, L = 0.8 m and H = 0.54 m are the channel width and water depth under the testing condition, respectively. Thus, the blockage ratio was approximately 16.4% in this study.

The TSR is defined as the ratio of the rotor tip velocity to the inflow velocity:

$$TSR = \frac{\omega R}{U_0} \tag{3}$$

where ω is the rotor angular velocity, with an averaged value of 132.6 rpm and a mean-square deviation of approximately 1.12 rpm, and $U_0 \approx 0.59$ m/s is the mean longitudinal velocity of incoming flow. Therefore, the TSR of this turbine was:

$$TSR = \frac{\omega R}{U_0} = \frac{132.6 \times 2\pi}{60} \times \frac{0.15}{0.59} \approx 3.53 \tag{4}$$

The thrust coefficient C_t is obtained from:

$$C_t = \frac{2F}{\rho A_t U_0^2} \tag{5}$$

where F is the thrust on the turbine rotor.

The power coefficient C_p is defined as the ratio of power P taken by the tidal steam turbine to the maximum available power P_0 from the incoming flow passing through the swept area:

$$C_p = \frac{P}{P_0} = \frac{T \cdot \omega}{\frac{1}{2}\rho A_t U_0^3} = \frac{F \cdot u_t}{\frac{1}{2}\rho A_t U_0^3} \tag{6}$$

where T is the torque on the turbine rotor, u_t is the mean velocity passing through the turbine rotor.

2.3. Velocity measurement

An Acoustic Doppler Velocimeter (ADV) was used to measure the time varying velocities; subsequently, the three-dimensional mean velocities and turbulent flow fields were obtained. The ADV was fixed on a platform that freely moved along the cross-section of the channel. The whole measurement system also moved along the flow direction. The ADV employed in this study had four 10 MHz receiving elements, one of which was marked with a red coil to show the direction of velocity component u. In this study, the velocity range was from 0.0 to 1.0 m/s, with measuring accuracy being within ±0.5% of the velocity. At each measurement point, velocity data were recorded for 60 s at a sampling rate of 200 Hz to ensure the accuracy of the time-averaged velocity and turbulence statistics. The ADV signal quality, represented by the signal to noise ratio (SNR) and correlation coefficient (COR), was tested prior to each set of measurements. The majority of the samples had SNR > 20 dB and COR > 90%, which indicated that the measurement data were reliable.

Velocity measurements were carried out at sixteen transverse sections from upstream to downstream of the turbine over the range x = (−1RD, 20RD), with a longitudinal spacing between sections increasing downstream (see Fig. 2a). Time varying velocities at thirteen transverse sections downstream were used to investigate the wake structure and turbulence flow field behind turbine rotor. In the vertical direction, measurements were collected at fifteen heights, with a regular spacing of 0.03 m. The top layer of the velocity measurements was submerged 0.07 m below the free surface, and the bottom layer was located at 0.05 m above the floor. In the span-wise direction, velocities were measured across the width of the channel at a lateral spacing of 0.025 m. The details of the measurement locations are illustrated in Fig. 2b, where 435 velocity samples were collected at each cross-section.

Table 1
Detailed blade profile description.

Location	Diameter (m)	Chord length (m)	Twist (deg)
Widest section	0.130	0.045	30
Blade tip	0.300	0.030	15

2.4. Flow characteristics

Time varying velocity u is recorded to determine the mean flow velocity and turbulence intensity:

$$u = \bar{u} + u' \tag{7}$$

where $\bar{u} = \frac{1}{N}\sum_{i=1}^{N} u_i$ is the time-averaged velocity, N is the number of velocity samples for 60 s and u' represents the fluctuating velocity.

The wake velocity deficit U_{def} is calculated as:

$$U_{def} = \left(1 - \frac{\overline{u_{tt}}}{\bar{u}}\right) \times 100\% \tag{8}$$

where $\overline{u_{tt}}$ is the time-averaged velocity at a location with turbine installation.

The dimensionless Reynolds shear stress R_{xy} is defined as:

$$R_{xy} = \frac{\sqrt{\left|\frac{1}{N}\sum_{i=1}^{N}(u_i - \bar{u}_i)(v_i - \overline{v_i})\right|}}{U_0} \tag{9}$$

The dimensionless longitudinal turbulence intensity I_x is defined as:

$$I_x = \frac{\sqrt{\frac{1}{N}\sum_{i=1}^{N}(u_i - \overline{u_i})(u_i - \overline{u_i})}}{U_0} \times 100\% \tag{10}$$

Similarly, the time-averaged velocities $(\bar{v}, \bar{w})$, Reynolds shear stresses (R_{yz}, R_{xz}) and turbulence intensities (I_y, I_z) can also be computed in the same way.

Before the turbine was installed, velocity measurements were conducted at two cross-sections, i.e., at -4RD and 4RD downstream. The profiles of the time-averaged velocities at the two cross-sections were very similar, as shown in Fig. 3. In the lateral direction, the longitudinal velocities were approximately uniform over the range $-0.25\text{ m} \le Y \le 0.25$ m, and the velocity ranged from 0.57 to 0.61 m/s in the vertical direction when $Z > -0.15$ m. In the main flow region, the mean longitudinal velocity was 0.59 m/s. The value of Reynolds number of incoming flow in the open

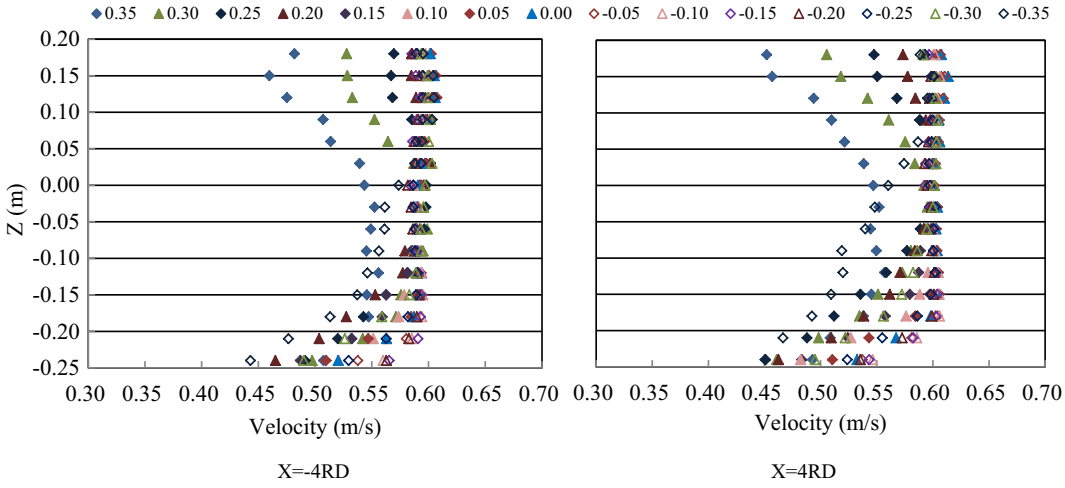

Fig. 3. Profiles of the time-averaged velocity at cross-sections upstream (-4RD) and downstream (4RD) of the turbine rotor. The number in legend shows the lateral location Y (m).

channel was Re = UH/v = 318600. As seen in Fig. 4, the values of the turbulence intensity at the two cross-sections mainly varied in the range of 2–8%, and a slightly stronger turbulence was seen close to the bottom and walls of the channel. Over the swept area, the inflow turbulence intensity was approximately 2%. Generally, both the velocity and turbulence intensity profiles were asymmetrical close to the flume walls in the transverse direction, while good symmetry was seen in the main flow region.

Secondary flows were observed near the water surface and channel walls, the maximum transverse velocity and vertical velocity at the cross sections were 0.034 m/s and 0.024 m/s, respectively. The components of the secondary flow at the cross-sections were generally less than $0.05U_0$, which had no significantly influence on the turbine rotation and wake development.

2.5. Performance of the turbine

The performance of a tidal stream turbine is typically characterised by the thrust coefficient and power coefficient. In this study, the flow thrust on the turbine rotor was measured by a full-bridge dynamic strain gauge, which was located at 0.5 RD downstream of the rotor plane and mounted on the hub end (shown in Fig. 5). The strain gauge was installed in a cylindrical case of the same diameter as the turbine hub. A stainless steel ball with a 0.01 m diameter was fixed on the central axis of the strain gauge and connected to a concave nut that rotated with the turbine rotor. The strain gauge was calibrated by the measurement of the strain capacity corresponding to the increments of static load, from 0.5 kg to 1.5 kg, applied to the steel ball. A good linear relationship was obtained between the applied load and measured strain capacity, with an error of approximately 1.0%. Thrust data were recorded via a strain gauge module with a bridge voltage of 10 V, and each record was collected for a 60 s duration at 200 Hz.

The flow velocities at the rotor cross-section were only measured outside of the rotor swept area, and the missing velocity values were determined by interpolation. Then the discharge inside of the swept area was obtained based on the concept of mass balance and the average velocity passing through the rotor was found 0.46 m/s. In the current study, the mean inflow velocity in the main flow region was 0.59 m/s and the measured average thrust of incoming flow on turbine rotor was 5.12 N. Using Eq. (5), it was found that the thrust coefficient was 0.41. Using Eq. (6), it was found the kinetic energy extracted by the tidal stream turbine was 2.36 W and the maximum available power from the incoming

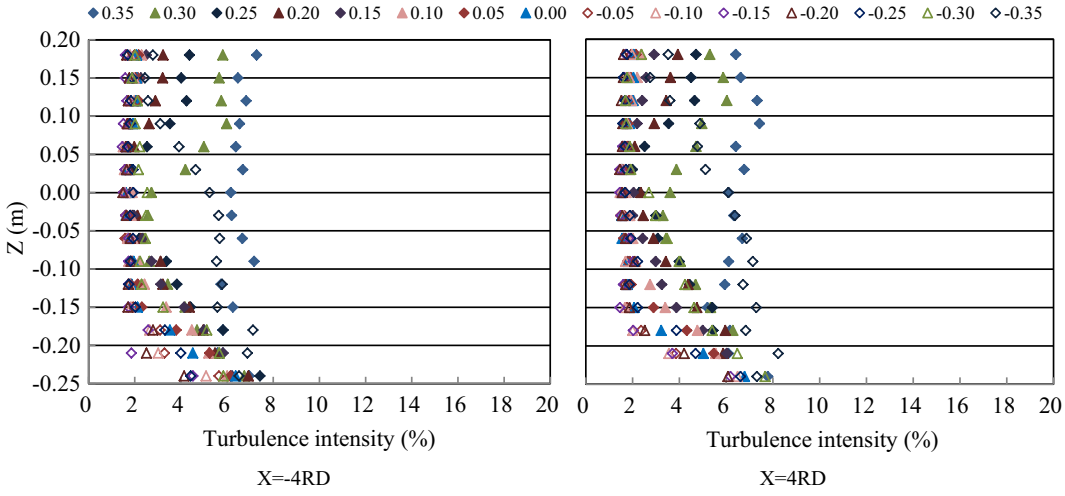

Fig. 4. Profiles of the longitudinal turbulence intensity at cross-sections upstream (-4RD) and downstream (4RD) of the turbine rotor. The number in legend shows the lateral location Y (m).

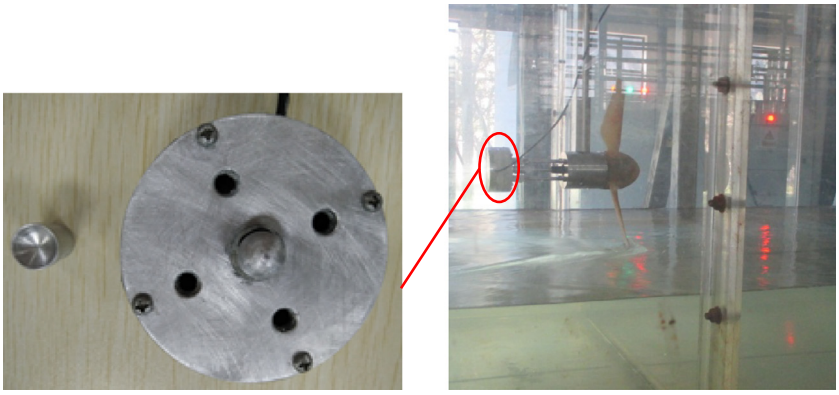

Fig. 5. Dynamic strain gauge and the equipment assembly of the thrust measurement.

flow passing through the swept area was 7.26 W. Therefore, the power coefficient was 0.33. As the angular velocity of turbine rotor was 13.88 rad/s, and the torque on turbine rotor was found to be 0.17 N m by Eq. (6).

The rotor's performance is influenced by the blockage ratio due to the acceleration of flow through and around the turbine rotor [44,45]. For blockage ratio below 10%, the turbine performance variation is small; but for blockage ratio beyond 10%, the performance is significantly improved as the TSR being higher than 4.0 [46]. In the current study, the blockage ratio was 16.4%, and the TSR was about 3.53. Thus blockage correction was necessary. There are two commonly adopted models for blockage correction, both of which were based the concept of 'equivalent free-expanded upstream flow' [47,48]. Bahaj et al. [47] proposed an upstream velocity that would lead to the same power extraction as that an unlimited cross-section, while Whelan et al. [48] substituted the velocity of incident flow with that of the bypass wake directly. In this study, the former method was adopted. Based on this method, the performance of the turbine rotor with the equivalent operating condition in an unconstrained flow were obtained. Correspondingly, the thrust coefficient and power coefficient were found to be 0.39 and 0.31, respectively.

3. Wake velocity deficit

3.1. Three-dimensional structure

The three-dimensional structure of the longitudinal velocity deficit shown in Fig. 6 was used to investigate the wake development. It was observed that a higher velocity deficit occurred close to the rotor axis, rather than the rotor blade tips, just downstream of the rotor, with a maximum velocity deficit of approximately 51.6% at X = 1RD. The velocity deficit rapidly recovered to 20% by 5.5RD downstream. Further recovery of the velocity deficit was gradual over the range of 5.5–10RD, with a deficit of 11.1% observed at 10RD downstream.

As seen from Fig. 6, there was also an obvious decrease in the velocity behind the turbine stanchion, with a velocity deficit of up to 25% at X = 1RD downstream. However, the velocity deficit induced by the blockage effects of the turbine stanchion rapidly decreased with the longitudinal distance. The whole wake developed into a nearly circular area by 4RD downstream, and the influence of the stanchion became negligible. Further downstream, a similar wake structure was maintained, while the velocity deficit decreased. The zone of the velocity deficit slightly expanded with

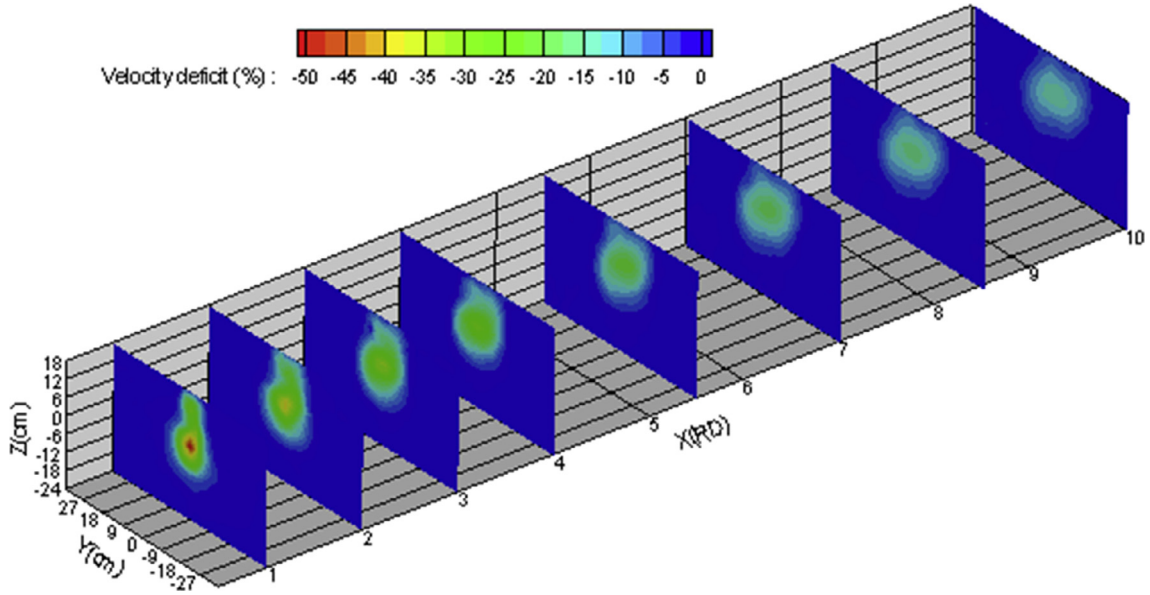

Fig. 6. Development of the wake structure at cross-sections over the range 1–10RD downstream.

the distance, and the radial gradient of the deficit was more uniform over the wake region. However, the rotor wake was narrowed in the vertical direction with distance due to the constraint of the free surface and channel bed.

3.2. Transverse development

The development of the velocity deficit at the Z = 0.0 m plane is presented in Fig. 7a. It is clear that the wake was approximately symmetrical near the centreline of the turbine rotor. The maximum velocity deficit was close to the rotor axis immediately downstream. Tedds et al. [41] showed that the largest velocity deficit behind the three-bladed turbine was around the blade tips of the rotor. The differences were mainly influenced by the TSR of the turbine rotor and blockage effects of the turbine hub. Corresponding to Fig. 6, a heavy flow disturbance induced by the rotor was seen at 1RD downstream. The rapid recovery of the velocity deficit was observed over the range of 1–5.5RD, followed by a slower recovery. It was almost maintained at a constant 5% beyond 18RD downstream.

From 1RD to 5.5RD, a near Gaussian profile was observed in the velocity deficit distribution along the transverse direction. Further downstream, the transverse profile became much more uniform. As shown in Fig. 7a, a bypass flow with a velocity deficit occurred around the rotor immediately downstream. The wake strip became narrower in the transverse direction within 5.5RD downstream, and then, this strip was slightly enlarged, with less diffusion over the distance 5.5–20RD downstream. The final width of the wake was approximately 1.5 times that of the rotor diameter at 20RD. The wake shape was influenced by the ambient turbulence, i.e., the wake strip was larger and more diffuse for ambient flow with a higher turbulence intensity than that with a lower one [39]. In the current study, the ambient turbulence intensity in the main flow region was about 2%, and the lateral expansion of the wake strip was small.

3.3. Vertical recovery

In contrast to the symmetric transverse profile, the velocity deficit profile at the Y = 0.0 m plane was asymmetrical near the rotor centreline, as shown in Fig. 7b. At 1RD downstream, the maximum deficit was located at the centreline of the turbine rotor, while a velocity reduction was also observed above the centreline in the vertical direction. The deficit value was up to 25% at Z = 0.12 m due to the combined actions of the energy extraction by the turbine and blockage effects of the turbine stanchion. However, the velocity deficit induced by the turbine stanchion rapidly recovered and the two wakes merged to form a single wake from 3RD downwards. Interestingly, its centreline tilted slowly towards the water surface as the wake moved downstream. As shown in Fig. 4, the turbulence strength of the ambient flow, without the turbine, was nearly uniform along the water depth above Z = −0.15 m, which cannot result in a faster recovery of the velocity deficit below the rotor axis. In addition, the effect of the turbine rotation

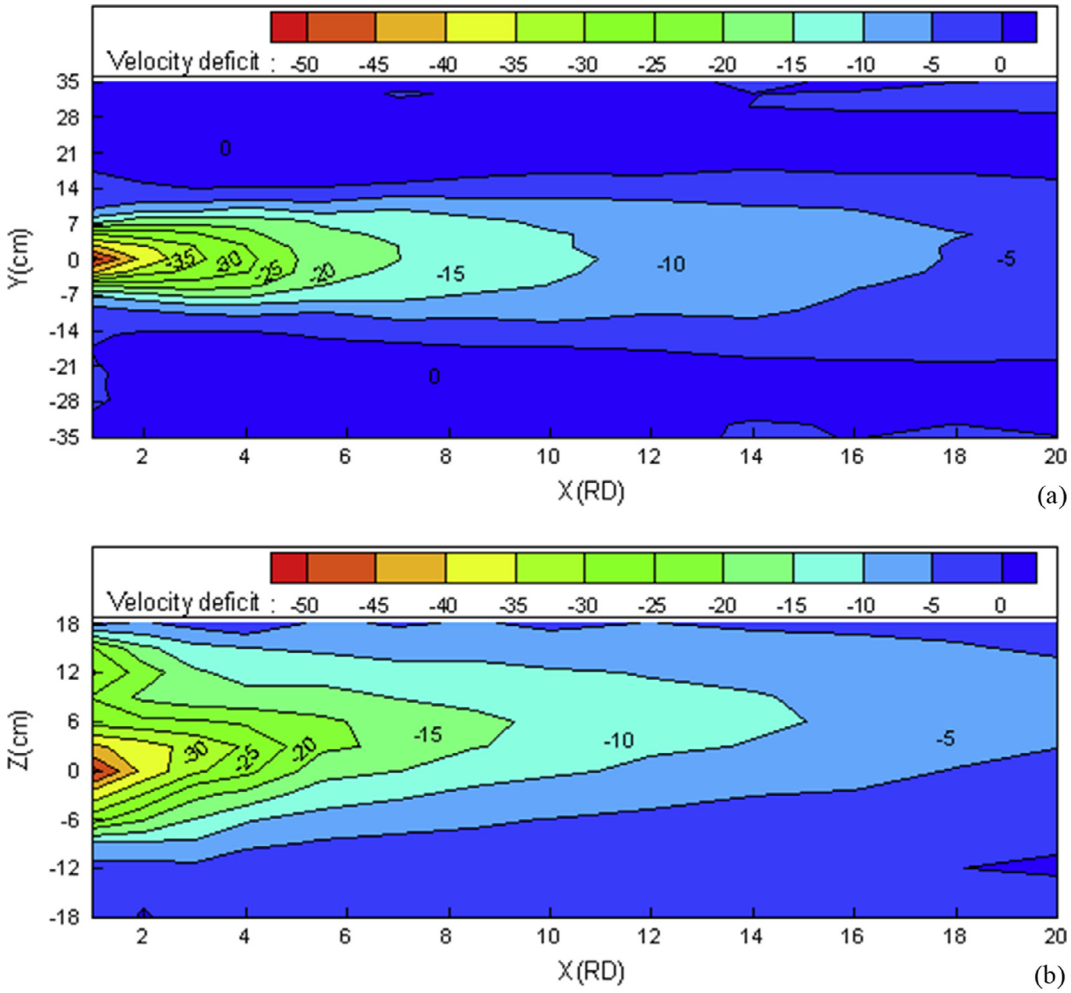

Fig. 7. Profiles of the velocity deficit at the (a) Z = 0.0 m and (b) Y = 0.0 m plane downstream of the turbine rotor.

on the wake recovery was small beyond 3RD downstream (see Section 4). In the current study, the stanchion caused an obvious velocity deficit above the turbine rotor, the initial upwards movement of the wake was considered to be mainly caused by merging the two wakes. However, the surface proximity could also result in the upward movement [16].

3.4. Blockage effects

The blockage correction revealed that the high blockage ratio improved the performance of the rotor. The effect of blockage on the characteristics of wake velocity deficit is shown in Fig. 8. At the rotor plane (X = 0RD), the bypass flow accelerated significantly, with the maximum increment of flow velocity being approximately 6.5% around the rotor tips (see in Fig. 8a). At Y = ±0.25RD, the velocity deficit was higher within the distance 2–5.5RD than that immediately downstream. While at Y = ±0.5RD the flow accelerated within the distance 2–5.5RD, and the velocity increment was up to 1.12% (Fig. 8b). As shown in Fig. 7a, the wake strip behind the rotor became narrowed in the transverse direction within 5.5RD downstream. This was due to the higher speed flow around the rotor, which caused strong wake mixing in the shear stress layer over the distance 2–5.5RD downstream. Beyond 0.6RD in lateral direction, the flows almost accelerated along the longitudinal distance downstream. Compared to the study of Stallard et al. [38], with blockage ratio being 2.5%, the wake strip behind turbine rotor was narrower in this study.

4. Wake rotation

As presented in Fig. 9, the wake rotation caused by the turbine rotor was observed within the region of the longitudinal velocity

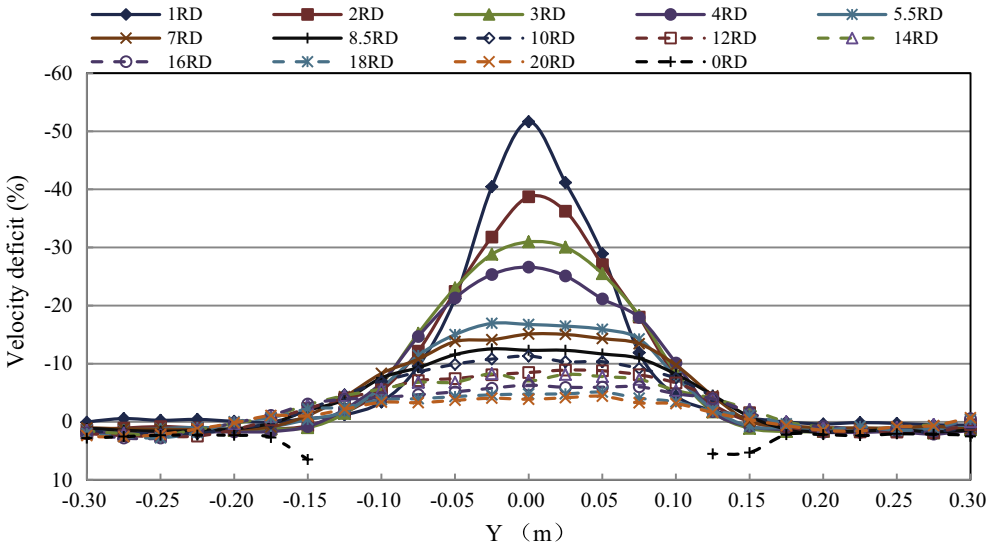

(a) Lateral profiles of velocity deficit, the legend above the figure denotes the longitudinal distance from turbine rotor cross-section

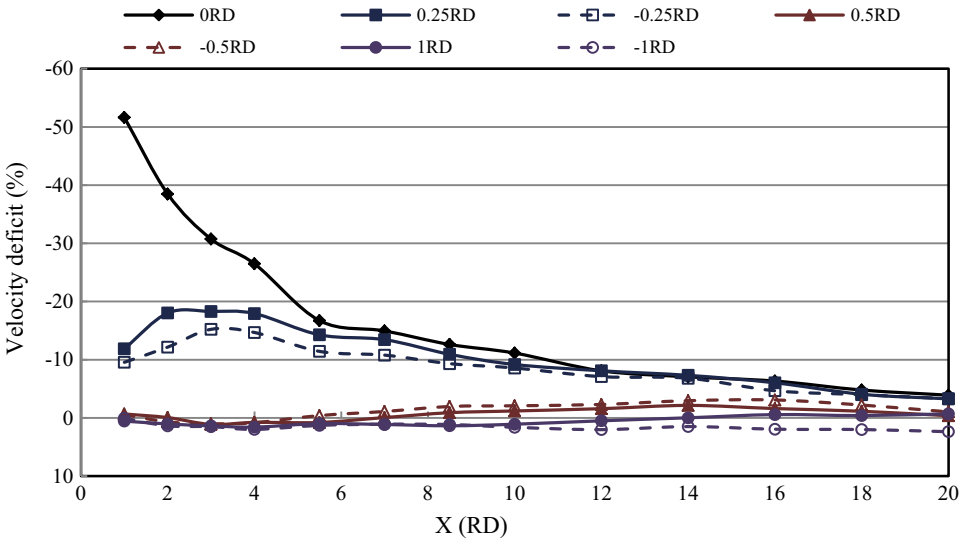

(b) Longitudinal variation of velocity deficit, the legend above the figure denotes the lateral distance from turbine central axis.

Fig. 8. Lateral profiles and longitudinal variation of velocity deficit.

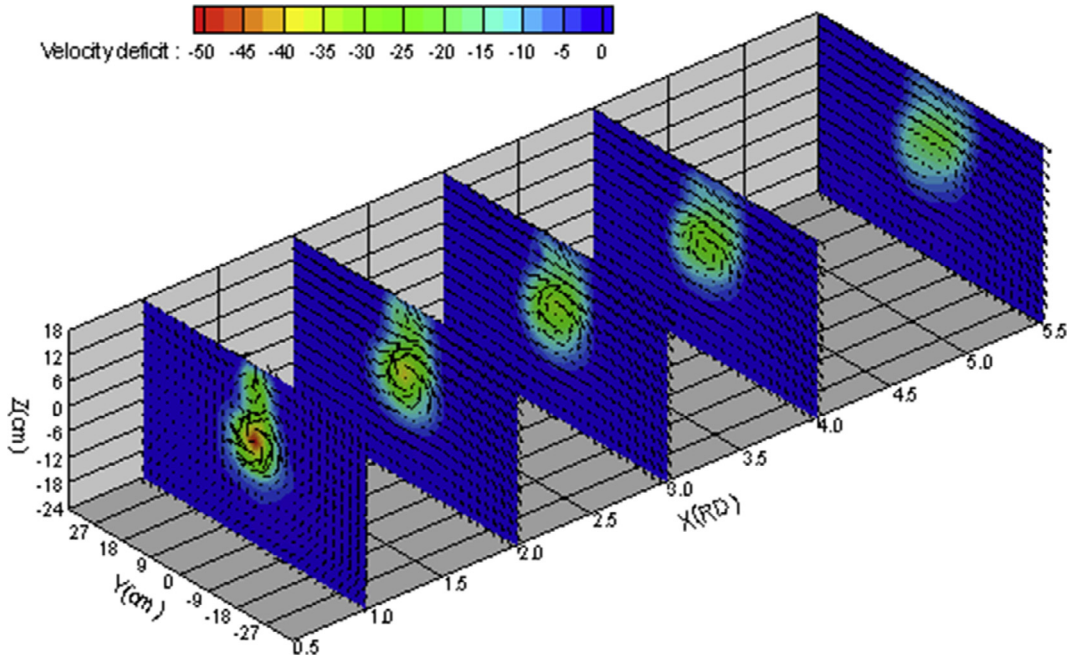

Fig. 9. Development of wake rotation in the cross-sections downstream. The colour variance represents the deficit of the longitudinal velocity, and the arrowhead represents the circulation vector.

deficit over the range 1–4RD downstream. In the vertical plane, the anti-clockwise circumfluence was nearly symmetrical near the central axis of turbine rotor. Since the turbine hub was stationary, the circulation downstream only occurred in the region between the turbine hub and rotor tips. However, a secondary flow also appeared behind the turbine stanchion due to the blockage effects. Compared to the rotor wake rotation, the secondary flow behind the stanchion was relatively weak, rapidly decreased and was negligible by 3RD downstream.

The high tangential velocity was mainly located within a circular band of 0.03 m < R < 0.10 m at 1RD downstream. The distribution of the circumfluence velocity was non-uniform in the circular band, with a maximum tangential velocity of approximately 20% of the stream-wise flow (see Fig. 10). Over the interval 1–2RD, the wake rotation speed rapidly reduced and the velocity distribution became more uniform at 2RD. The rotation region slightly expanded outwards and shifted upwards with distance, which played an important role in the process of wake propagation. At 1RD downstream, entrainment of the surrounding flow is observed between the rotating wake and ambient flow. Further downstream, the entrainment decreased and the transverse velocity of the ambient flow increased in the vertical plane, which indicated that the process of wake mixing between turbine wake and the ambient flow occurred. As shown in Fig. 10, the ambient flow with a high tangential velocity entered the wake zone from one side of the rotor, while the wake flow with a low tangential velocity entered the ambient flow from another side. Similar to the velocity deficit recovery, the circumfluence behind the turbine rotor rapidly decreased in the near wake, and no obvious wake rotation was observed in the velocity deficit area after 5.5RD downstream.

5. Wake turbulence

5.1. Turbulence intensity

The ambient turbulence intensity had effects on the behaviour of the horizontal axis turbine, its performance fluctuations dramatically increased with high turbulence intensity [40]. In addition, the wake shape, length and strength were also influenced by the ambient flow turbulence intensity. Therefore, the wake turbulence of an upstream turbine may affect the performance and wake recovery of other turbine located downstream. This study investigated the wake turbulence intensity of a horizontal axis turbine to further understand the process of wake mixing.

5.1.1. Three-dimensional structure

The distribution of the longitudinal turbulence intensity I_x behind the rotor is shown in Fig. 11. Immediately downstream, a higher turbulence intensity was observed above the central axis of the rotor due to both the rotor rotation and appearance of the turbine stanchion, with a maximum turbulence intensity of approximately 23%. Similar to the velocity deficit, the effect of the stanchion on the turbulence intensity sharply decreased over the distance of 1–2RD downstream, and the turbulence intensity was almost uniform over the wake zone at 2RD downstream. With the distance increasing downstream, the area of the turbulence intensity slightly extended in the transverse direction and shifted from the water surface towards the wake core. The region of turbulence intensity approached a circle by 5.5RD and further spread outwards in the transverse direction over the range of 5.5–10RD. Compared to the ambient turbulence with turbine absence (Fig. 4), the turbulence intensity close to the channel bed and walls was not significantly influenced by the presence of the rotor within 10RD downstream.

5.1.2. Decay in planes

The distribution of the turbulence intensity in the x-y plane, at Z = 0.0 m, is presented in Fig. 12a. Close to the blade tips, the turbulence intensity was generally expected to be higher than that at other areas due to the maximum speed of the rotor blade and generation of tip vortices. However, for a low TSR, a higher turbulence intensity area was located close to the wake core, with a maximum turbulence intensity of approximately 15.5% at 1RD downstream. The value of the turbulence intensity was rapidly reduced within 4RD downstream, with a gradual decrease further downstream.

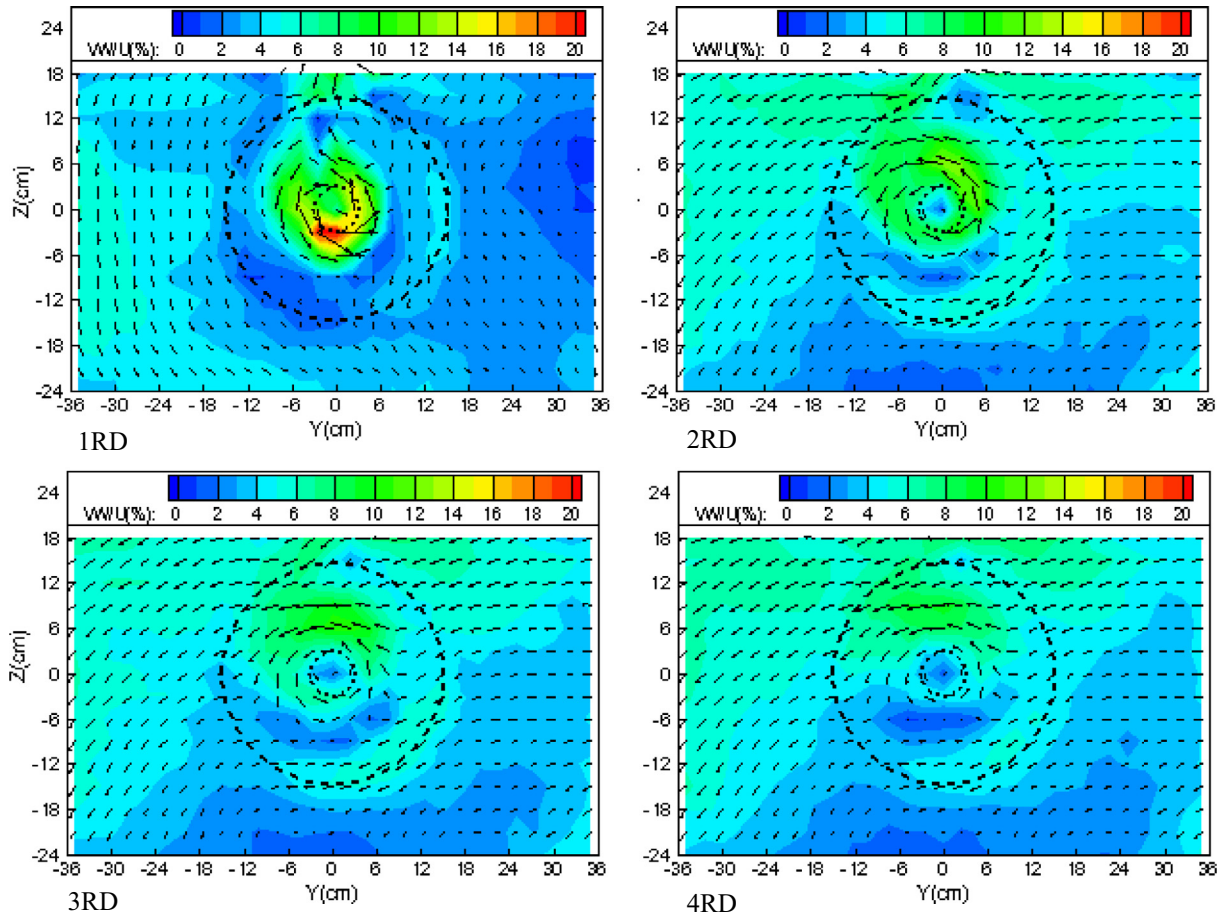

Fig. 10. Tangential velocity of wake rotation in the cross-sections at X = 1RD, 2RD, 3RD and 4RD downstream of the turbine rotor. The dashed curve denotes the rotor radius, and the dotted curve denotes the hub radius.

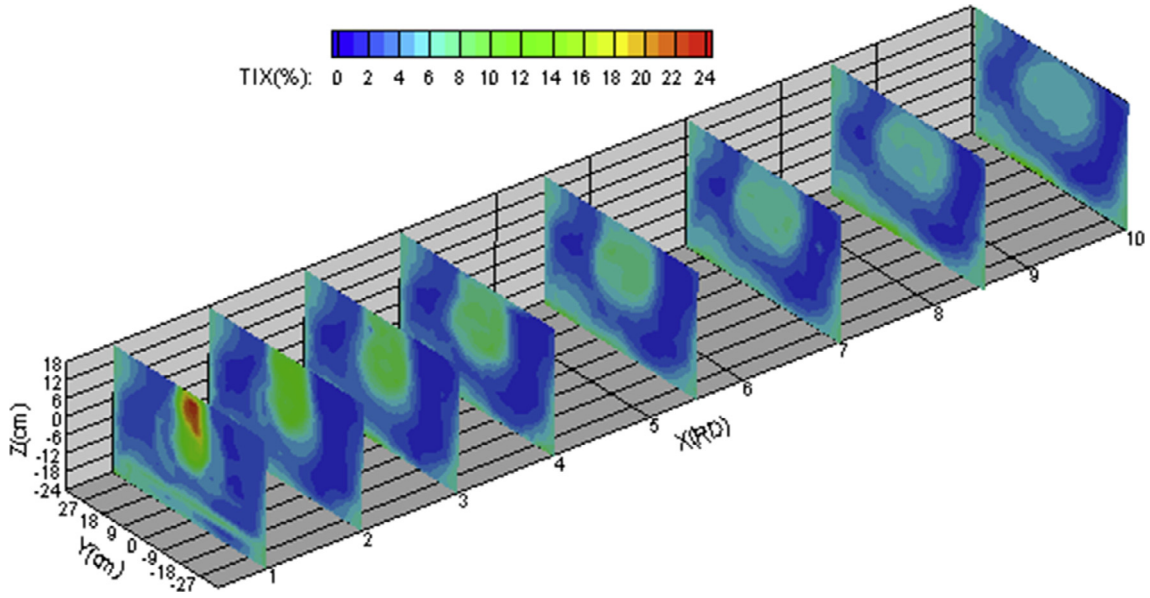

Fig. 11. Three-dimensional structure of the longitudinal turbulence intensity at cross-sections over the range of 1–10RD downstream.

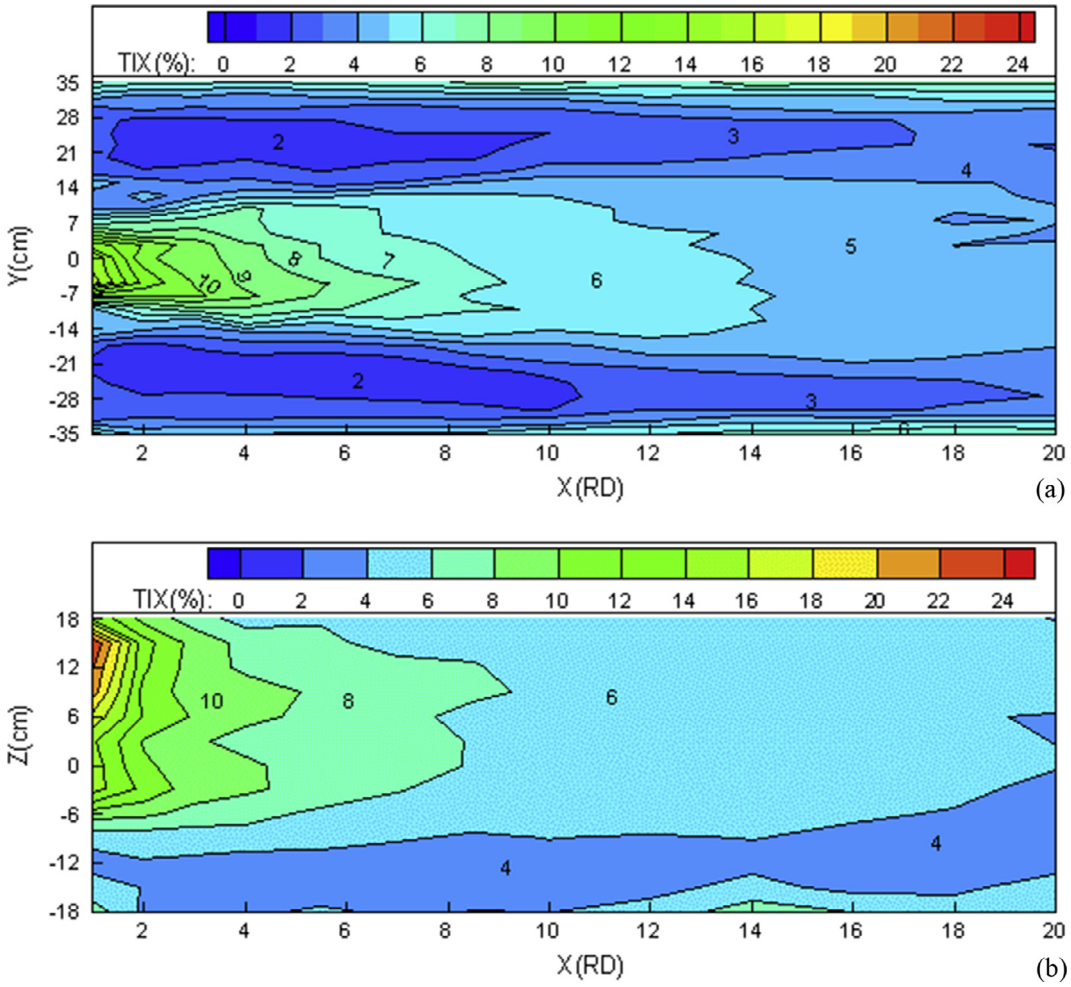

Fig. 12. Profiles of the longitudinal turbulence intensity at (a) Z = 0.0 m and (b) Y = 0.0 m downstream of the turbine rotor.

The turbulence intensity did not fully recover to the ambient turbulence conditions, even at 20RD, where the turbulence intensity was approximately 5%, which was higher than the intensity without the turbine. The strip of high turbulence intensity expanded in the transverse direction and almost reached the full width of the channel at 20RD downstream. This indicated that the ambient turbulence resulting from the turbine had a significant effect on the performance fluctuation and wake characteristics of turbines located downstream, as well as two sides.

The change of the turbulence intensity distribution in the *x-z* plane, at Y = 0.0 m, is shown in Fig. 12b. The strongest turbulence appeared at Z = 0.15 m in the vertical direction immediately behind the turbine, which was probably due to the rotor tip vortices and the presence of the stanchion. A smaller peak was seen around the wake centreline at 1RD downstream. Consistent with Fig. 11, the turbulence intensity rapidly decreased within 2RD downstream. Two peaks moved towards to each other and merged to form a single peak, and the turbulence intensity was more uniform with distance. However, no obvious expansion of the turbulence intensity strip was seen in the vertical direction, and the strip became narrowed along the water depth further downstream.

5.2. Reynolds shear stress

The wake turbulence was anisotropic due to blade rotation and presence of a support structure. Numerical model simulations were conducted to study the turbine wake using a standard turbulence model based on an isotropic turbulence assumption, which could not exactly capture the turbulent flow fields in the near-weak [23]. Therefore, it is crucial to have insight into the turbulence anisotropy induced by tidal stream energy extraction. The Reynolds shear stress is usually used to characterise the degree of turbulence anisotropy.

The distribution of Reynolds shear stress R_{xy} at cross-sections behind the rotor is depicted in Fig. 13. The large Reynolds shear stress R_{xy} was located in the area around the rotor hub and turbine stanchion, with a maximum Reynolds shear stress R_{xy} of approximately 0.11 at 1RD downstream. Then, the area of the Reynolds shear stress R_{xy} in the turbine wake broke down into two, but the shapes of these two areas were asymmetrical around the Y = 0.0 m plane. The Reynolds stress R_{xy} reduced along the distance in both of these two areas, but with different decay rates. The maximum value of the shear stress R_{xy} was approximately 0.04 at 10RD downstream, which indicated that the turbulent flow was still not fully recovered.

The distribution of Reynolds shear stress R_{xy} in the *x-y* plane (Z = 0.0 m) is presented in Fig. 14a. Two similar peaks of Reynolds shear stress R_{xy} occurred close to the rotor hub at 1RD behind the turbine rotor. The maximum shear stress was approximately 0.08, i.e., the turbulent flow fields were very anisotropic downstream of the turbine hub. The shear layer was very thin just behind the rotor and was less than one diameter at 1RD downstream. With the longitudinal distance increasing, the shear layer naturally developed and spread almost linearly outwards in the transverse direction,

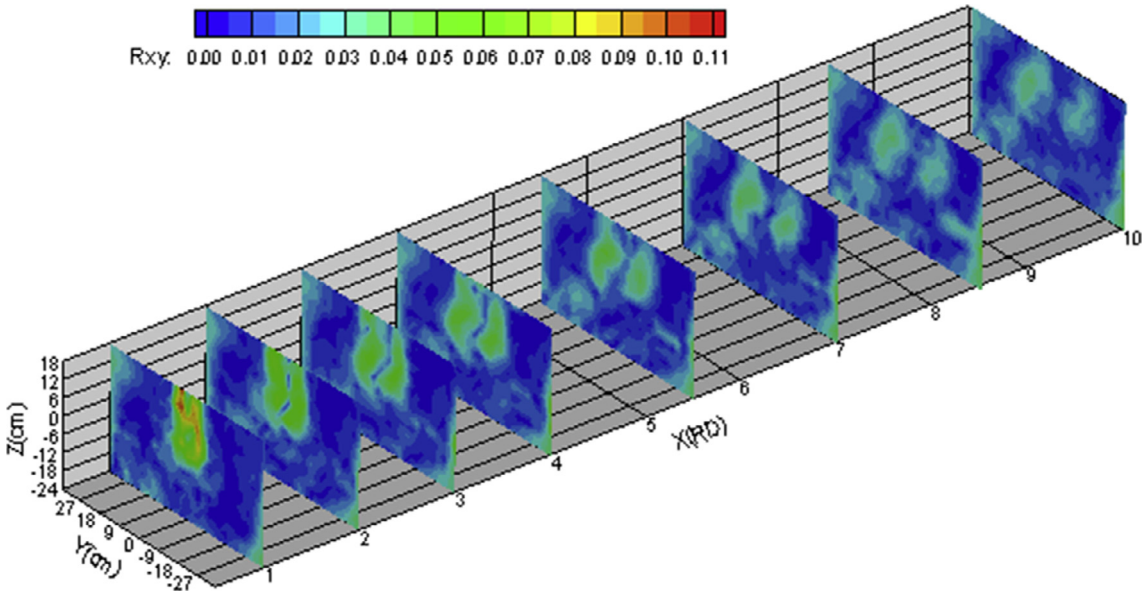

Fig. 13. Distributions of the Reynolds shear stress R_{xy} at cross-sections downstream of the turbine rotor.

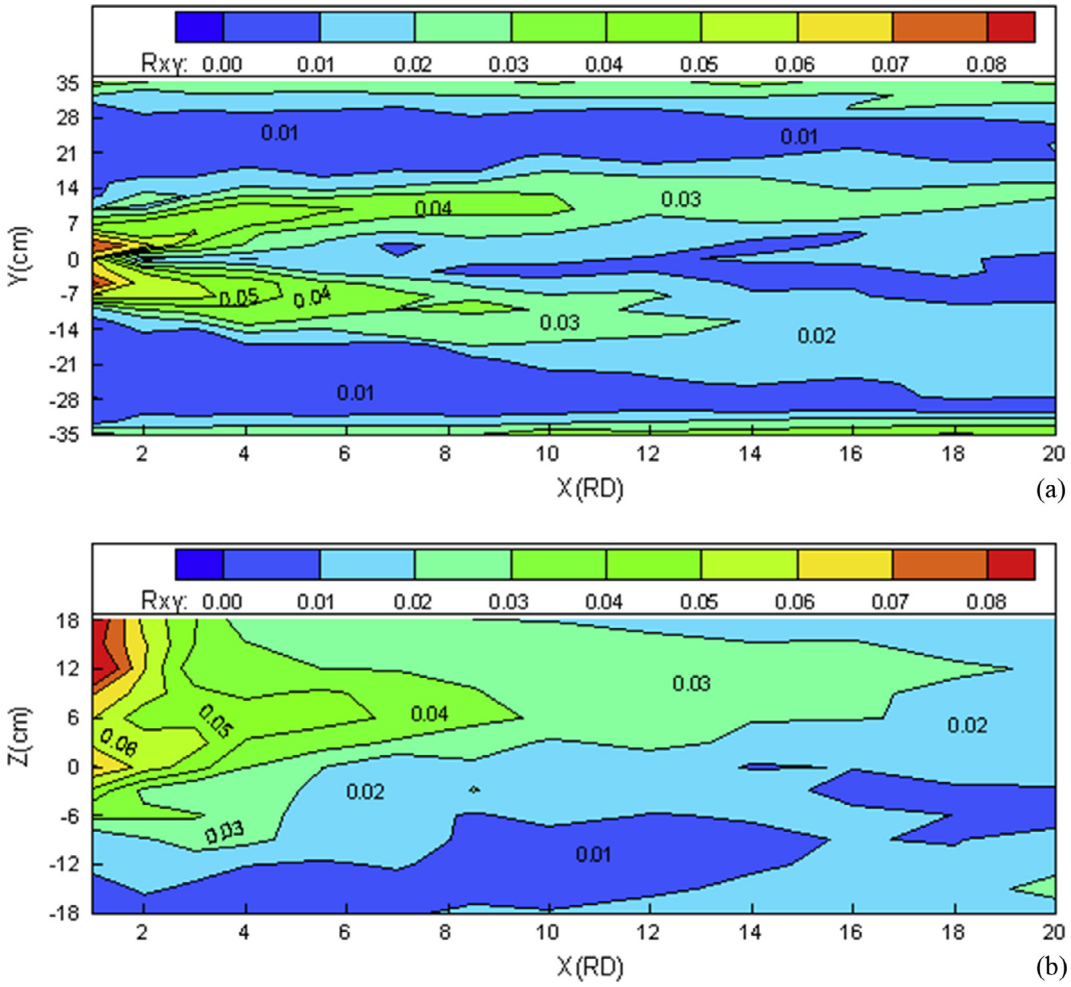

Fig. 14. Profiles of Reynolds shear stress at (a) Z = 0.0 m and (b) Y = 0.035 m downstream of the turbine rotor.

which meant that the degree of turbulence anisotropy decreased while the influence area expanded.

As shown in Fig. 13, the highest Reynolds shear stress R_{xy} was located at Y = ±0.035 m, rather than at the turbine centre Y = 0.0 m. To further investigate the characteristics of turbulence anisotropy, the vertical profile of the Reynolds shear stress R_{xy} at Y = 0.035 m is presented in Fig. 14b. Along the vertical direction, two Reynolds shear stress R_{xy} peaks were observed at 1RD downstream, with peak values of approximately 0.11 and 0.06, respectively. Over the range of 1–3RD, the peaks values rapidly decreased, especially for that induced by the stanchion. In the vertical direction, the two peaks merged along the distance and eventually formed into a single shear layer at 4RD downstream. The shear layer also seemed to move upwards further downstream. The distributions of Reynolds shear stresses R_{yz} and R_{zx} behind the turbine rotor are given in Appendix A and B, respectively.

6. Discussion

In terms of tidal stream energy extraction, it is important to understand the wake characteristics of an isolated turbine because the unsteady loading and performance of other turbines in a turbine array are influenced by the upstream wake, which also determines the optimized configuration of multi-turbines [49]. A perforated disc was employed to investigate the wake propagation, but the decay rate of the turbulent kinetic energy may be greater than using a turbine rotor because the swirl effects of the turbine rotor are neglected.

Using a model tidal stream turbine, the near-wake structure of a horizontal axis rotor was studied over the range 2–7 RD [41]. The maximum velocity deficit occurred immediately downstream of the rotor blade tips, rather than at the centre axis of the rotor, which was different from our experiment results due to the difference in TSR and hub blockage. Similar to our results, Tedds et al. [41] also showed that the wake turbulence induced by the blade rotation was anisotropic and the turbulence models based on the isotropic concept could not accurately capture the turbulence features. Constrained vertically by the free surface and channel bed, the turbulence structure behind the turbine rotor was also anisotropic far wake, and the horizontal length was many times the vertical length [50]. This was a limitation of our study, where the channel width scale was approximately 1.6 times the depth and the horizontal development of the turbulence structure in the far wake could be influenced by the channel width.

The motion of tip vortices affected the wake mixing. The near wake rotation of the horizontal axis turbine was observed in our experimental investigation, as well as the study of Stallard et al. [42]. At 1 RD downstream, our study showed that the distribution of the circumfluence velocity was non-uniform in a circular band, and the maximum tangential velocity, which was approximately 20% of the stream-wise velocity, was located below the rotor central axis. The high tangential velocity was nearly uniformly distributed within a circular band at 1 RD in Stallard's study. The non-uniformity of wake rotation resulted in a different degree of wake mixing behind the turbine rotor and may further affect the wake recovery rate of the near wake in the vertical direction. However, existing physical experiments studying on the development of three-dimensional wake structure downstream are very limited, which makes it very difficult to have a like to like comparison. Therefore, further investigation on the wake development behind tidal turbine is necessary.

From the experiments we have obtained improved understanding of the wake characteristics, including velocity deficit, wake rotation and wake turbulence over the full wake length. These results could be used, for example, in arranging a turbine array to avoid energy reduction caused by wakes interaction. For the case of a relatively small ambient turbulence intensity and high blockage ratio, the lateral spacing between two turbine axes in an array is 1.5RD, and then the longitudinal distance between two rows should be longer than 5RD due to wake rotation upstream. However, if the array is staggered arrangement, then the longitudinal distance between two rows should be shorter than 12RD because the wake turbulence intensity spreads in the transverse direction.

7. Conclusions

The performance of tidal stream turbines located in a turbine array is influenced primarily by the upstream wake. A good understanding of the full wake structure of a single turbine is crucial to optimize the arrangement of a tidal turbine array in the next stage. The process of wake recovery of a model horizontal axis turbine with three blades was experimentally studied. Detailed ADV measurements were undertaken at sixteen cross sections from 1 RD upstream to 20 RD downstream to investigate the wake structure along the full length of the turbine wake. The three-dimensional characteristics of the wake velocity deficit, wake rotation and wake turbulence behind the tidal stream turbine were obtained.

The mean velocity deficit downstream of the turbine was mainly induced by the kinetic energy extraction and the blockage effects of the turbine rotor and stanchion. With a low TSR of turbine rotor, the maximum velocity deficit was located at the wake core in the near wake. Wake rotation occurred immediately downstream, and the circumfluence velocity was up to 20% of the stream-wise flow velocity, which had a significant impact on the process of wake mixing. The wake strip was slightly enlarged and less diffuse in the transverse direction, as the ambient turbulence intensity was low and blockage ratio of the rotor was high. In the vertical direction, two wakes induced by turbine rotation and stanchion rapidly merged to form a single wake, and its centreline tilted slowly towards the water surface as the wake moved downstream.

For the far wake, both the turbulence intensity and Reynolds shear stress behind the turbine spread laterally, but expansion along the water depth was limited. This indicated that the turbulence strength and anisotropy resulting from a turbine would affect the performance of other turbines located both downstream and on two sides. In addition, the characteristics of the wake structure immediately downstream were considerably influenced by the turbine stanchion, but the effects were only limited in the near wake.

The originality of the paper was that this was the first experimental study to systematically investigate the three-dimensional characteristics of the whole wake structure of a three-blade turbine rotor, which enhanced the understanding of the evolution process of the three-dimensional wake structure. Furthermore, the study provided the details of the extent of rotating flow and anisotropic wake turbulence structure, as well as the distributions of Reynolds stresses.

Acknowledgements

This study was funded by the National High-tech Research and Development Program in China (863 Torch Program, 2012AA052602).

Appendix A. Reynolds shear stress R_{yz}

Fig. A.15 presents the distributions of Reynolds shear stress R_{yz} at cross-sections by 10RD downstream, with the maximum Reynolds stress being up to 0.08 at 1RD downstream.

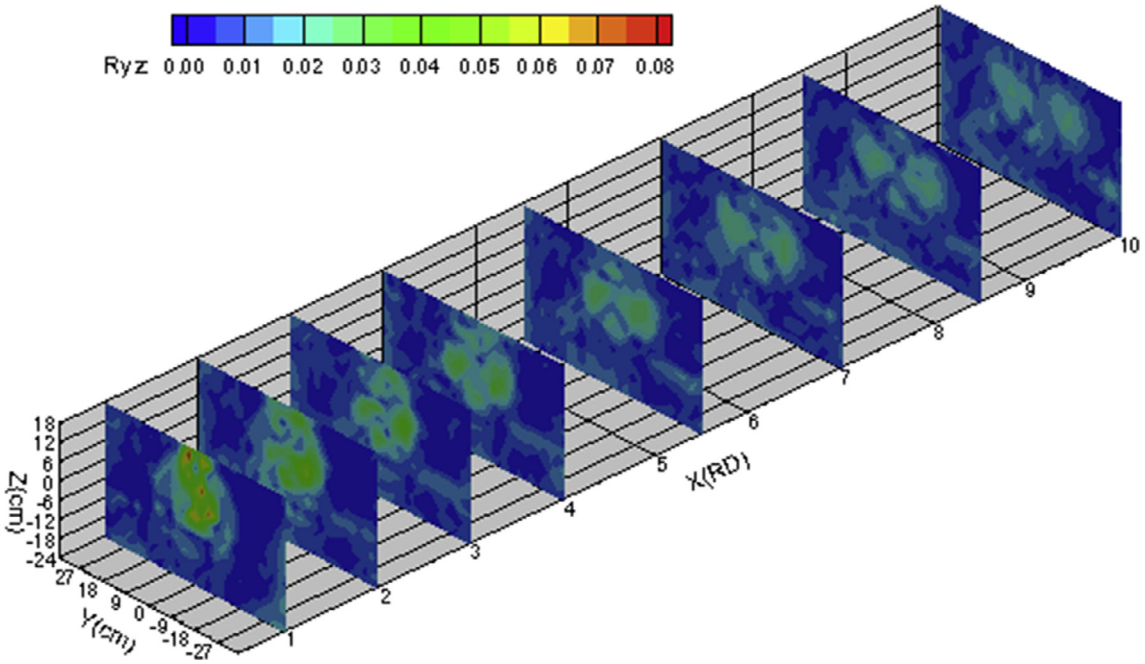

Fig. A.15. Distributions of the Reynolds shear stress R_{yz} at cross-sections downstream of the turbine rotor.

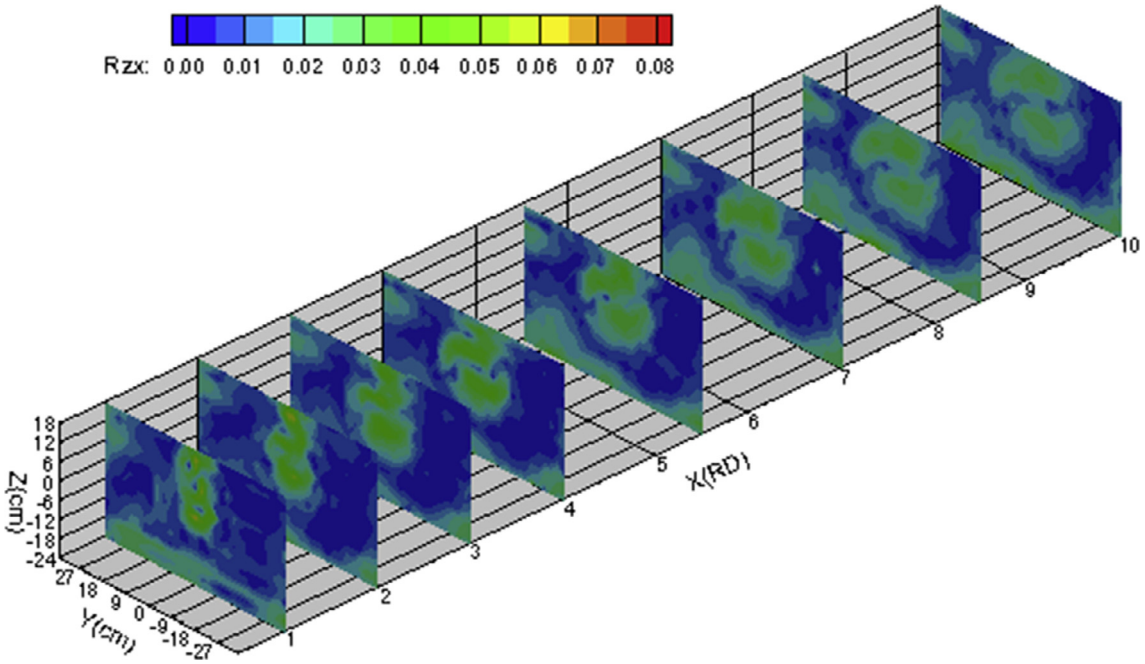

Fig. B.16. Distributions of the Reynolds shear stress R_{zx} at cross-sections downstream of the turbine rotor.

Appendix B. Reynolds shear stress R_{zx}

Fig. B.16 presents the distributions of Reynolds shear stress R_{zx} at cross-sections by 10RD downstream, with the maximum Reynolds stress being up to 0.065 at 1RD downstream.

References

[1] Zupone G, Amelio M, Barbarelli S, Florio G, Scornaienchi N, Cutrupi A. Lcoe evaluation for a tidal kinetic self balancing turbine: case study and comparison. Appl Energy 2017;185:1292–302. http://dx.doi.org/10.1016/j.apenergy.2016.01.015.

[2] Lewis M, Neill S, Robins P, et al. Resource assessment for future generations of tidal-stream energy arrays. Energy 2015;83:403–15. http://dx.doi.org/10.1016/j.energy.2015.02.038.

[3] Rourke F, Boyle F, Reynolds A. Tidal energy update 2009. Appl Energy 2010;87:398–409. http://dx.doi.org/10.1016/j.apenergy.2009.08.014.

[4] Zhou Z, Benbouzid M, Charpentier J, Scuiller F, Tang T. Developments in large marine current turbine technologies – A review. Renew Sustain Energy Rev 2017;71:852–8. http://dx.doi.org/10.1016/j.rser.2016.12.113.

[5] Brutto O, Thiebot J, Guillou S, Gualous H. A semi-analytic method to optimize tidal farm layouts – Application to the Alderney Race (Raz Blanchard), France. Appl Energy 2016;183:1168–80. http://dx.doi.org/10.1016/j.apenergy.2016.09.059.

[6] Robins P, Neill S, Lewis M, Ward S. Characterising the spatial and temporal variability of the tidal-stream energy resource over the northwest European

shelf seas. Appl Energy 2015;147:510–22. http://dx.doi.org/10.1016/j.apenergy.2015.03.045.
[7] Betz A. Das maximum der theoretisch möglichen Ausnutzung des windes durch wind motoren. Gesamte Turbinenwesen 1920;17:307–9.
[8] Pacheco A, Ferreira O. Hydrodynamic changes imposed by tidal energy converters on extracting energy on a real case scenario. Appl Energy 2016;180:369–85. http://dx.doi.org/10.1016/j.apenergy.2016.07.132.
[9] Vennell R. Tuning tidal turbines in-concert to maximize farm efficiency. J Fluid Mech 2011;671:587–604. http://dx.doi.org/10.1017/S0022112010006191.
[10] Vennell R. Realizing the potential of tidal currents and the efficiency of turbine farms in a channel. Renew Energy 2012;47:95–102. http://dx.doi.org/10.1016/j.renene.2012.03.036.
[11] Vennell R. Exceeding the Betz limit with tidal turbines. Renew Energy 2013;55:277–85. http://dx.doi.org/10.1016/j.renene.2012.12.016.
[12] Chen Y, Lin B, Lin J. Modelling tidal current energy extraction in large area using a three-dimensional estuary model. Comput Geosci 2014;72:76–83. http://dx.doi.org/10.1016/j.cageo.2014.06.008.
[13] Vennell R. The energetics of large tidal turbine arrays. Renew Energy 2012;48:210–9. http://dx.doi.org/10.1016/j.renene.2012.04.018.
[14] Chen Y, Lin B, Lin J, Wang S. Effects of stream array configuration on tidal current energy extraction near an island. Comput Geosci 2015;77:20–8. http://dx.doi.org/10.1016/j.cageo.2015.01.008.
[15] Fallon D, Hartnett m, Olbert A, Nash S. The effects of array configuration on the hydro-environmental impacts of tidal turbines. Renew Energy 2014;64:10–25. http://dx.doi.org/10.1016/j.renene.2013.10.035.
[16] Consul CA, Willden RHJ, McIntosh SC. Blockage effects on the hydrodynamic performance of a marine cross-flow turbine. Phil Trans R Soc A 2013;2013 (371):20120299. http://dx.doi.org/10.1098/rsta.2012.0299.
[17] Milne IA, Sharma RN, Flay RGJ, Bickerton S. Characteristics of the turbulence in the flow at a tidal stream power site. Phil Trans R Soc A 2013;2013 (371):20120196. http://dx.doi.org/10.1098/rsta.2012.0196.
[18] Ramos V, Carballo R, Alvarez M, Sanchez M, Iglesias G. Assessment of the impacts of tidal stream energy through high-resolution numerical modelling. Energy 2013;61:541–54. http://dx.doi.org/10.1016/j.energy.2013.08.051.
[19] Morandi B, Felice F, Costanzo M, Romano G, Dhome D, Allo J. Experimental investigation of the near wake of a horizontal axis tidal current turbine. Int J Marine Energy 2016;14:229–47. http://dx.doi.org/10.1016/j.ijome.2016.02.004.
[20] Fernandez-Rodriguez E, Stallard T, Stansby P. Experimental study of extreme thrust on a tidal stream rotor due to turbulent flow and with opposing waves. J Fluids Struct 2014;51:354–61. http://dx.doi.org/10.1016/j.jfluidstructs.2014.09.012.
[21] Pinon G, Mycek P, Germain G, Rivoalen E. Numerical simulation of the wake of marine current turbines with a particle method. Renew Energy 2012;46:111–26. http://dx.doi.org/10.1016/j.renene.2012.03.037.
[22] Mycek P, Gaurier B, Germain G, Pinon G, Rivoalen E. Numerical and experimental study of the interaction between two marine current turbines. Int J Marine Energy 2013;1:70–83. http://dx.doi.org/10.1016/j.ijome.2013.05.007.
[23] Sun X, Chick JP, Bryden IG. Laboratory-scale simulation of energy extraction from tidal current. Renew Energy 2008;33:1267–74. http://dx.doi.org/10.1016/j.renene.2007.06.018.
[24] Mason-Jones A, O'Doherty DM, Morris CE, O'Doherty T. Influence of a velocity profile & support structure on tidal stream turbine performance. Renew Energy 2013;52:23–30. http://dx.doi.org/10.1016/j.renene.2012.10.022.
[25] Lam W, Chen L. Equations used to predict the velocity distribution within a wake from a horizontal-axis tidal-current turbine. Ocean Eng 2014;79:35–42. http://dx.doi.org/10.1016/j.oceaneng.2014.01.005.
[26] Lam W, Chen L, Hashim R. Analytical wake model of tidal current turbine. Energy 2015;79:512–21. http://dx.doi.org/10.1016/j.energy.2014.11.047.
[27] Brutto O, Nguyen V, Guillou S, Thiebot J, Gualous H. Tidal farm analysis using an analytical model for the flow velocity prediction in the wake of a tidal turbine with small diameter to depth ratio. Renew Energy 2016;99:347–59. http://dx.doi.org/10.1016/j.renene.2016.07.020.
[28] Shives M, Crawford C. Adapted two-equation turbulence closures for actuator disk RANS simulations of wind & tidal turbine wakes. Renew Energy 2016;92:273–92. http://dx.doi.org/10.1016/j.renene.2016.02.026.
[29] Morris C, O'Doherty D, Mason-Jones A, O'Doherty T. Evaluation of the swirl characteristics of a tidal stream turbine wake. Int J Marine Energy 2016;14:198–214. http://dx.doi.org/10.1016/j.ijome.2015.08.001.
[30] Myers L, Bahaj A. Experimental analysis of the flow field around horizontal axis tidal turbines by use of scale mesh disk rotor simulators. Ocean Eng 2010;37:218–27. http://dx.doi.org/10.1016/j.oceaneng.2009.11.004.
[31] Myers L, Bahaj A. An experimental investigation simulating flow effects in first generation marine current energy converter arrays. Renew Energy 2012;37:28–36. http://dx.doi.org/10.1016/j.renene.2011.03.043.
[32] Harrison ME, Batten WMJ, Myers LE, Bahaj AS. Comparison between CFD simulations and experiments for predicting the far wake of horizontal axis tidal turbine. IET Renew Power Gener 2010;4(6):613–27. http://dx.doi.org/10.1049/iet-rpg.2009.0193.
[33] Nguyen V, Guillou S, Thiebot J, Cruz A. Modelling turbulence with an Actuator Disk representing a tidal turbine. Renew Energy 2016;97:625–35. http://dx.doi.org/10.1016/j.renene.2016.06.014.
[34] Batten W, Harrison M, Bahaj A. Accuracy of the actuator disc-RANS approach for predicting the performance and wake of tidal turbines. Phil Trans R Soc A 2013;2013:371. http://dx.doi.org/10.1098/rsta.2012.0293.
[35] Neary VS, Gunawan B, Craig Hill, Chamorro LP. Near and far field flow disturbances induced by model hydrokinetic turbine: ADV and ADP comparison. Renew Energy 2013;60:1–6. http://dx.doi.org/10.1016/j.renene.2013.03.030.
[36] Jo CH, Lee JH, Rho YH, Lee KH. Performance analysis of a HAT tidal current turbines and wake flow characteristics. Renew Energy 2014;65:175–82. http://dx.doi.org/10.1016/j.renene.2013.08.027.
[37] Gebreslassie M, Sanchez S, Tabor G, Belmont M, Bruce T, Payne G, et al. Experimental and CFD analysis of the wake characteristics of tidal turbines. Int J Marine Energy 2016;16:209–19. http://dx.doi.org/10.1016/j.ijome.2016.07.001.
[38] Stallard T, Collings R, Feng T, Whelan J. Interactions between tidal turbine wakes: experimental study of a group of three-bladed rotors. Phil Trans R Soc A 2013;371:20120159. http://dx.doi.org/10.1098/rsta.2012.0159.
[39] Mycek P, Gaurier B, Germain G, Pinon G, Rivoalen E. Experimental study of the turbulence intensity effects on marine current turbines behavior. Part I: one single turbine. Renew Energy 2014;66:729–46. http://dx.doi.org/10.1016/j.renene.2013.12.036.
[40] Mycek P, Gaurier B, Germain G, Pinon G, Rivoalen E. Experimental study of the turbulence intensity effects on marine current turbines behavior. Part II: two interacting turbines. Renew Energy 2014;68:876–92. http://dx.doi.org/10.1016/j.renene.2013.12.048.
[41] Tedds S, Owen I, Poole R. Near-weak characteristics of a model horizontal axis tidal stream turbine. Renew Energy 2014;63:222–35. http://dx.doi.org/10.1016/j.renene.2013.09.011.
[42] Stallard T, Feng T, Stansby PK. Experimental study of the mean wake of a tidal stream rotor in a shallow turbulent flow. J Fluids Struct 2015;54:235–46. http://dx.doi.org/10.1016/j.jfluidstructs.2014.10.017.
[43] Atcheson M, MacKinnon P, Elsaesser B. A large scale model experimental study of a tidal turbine in uniform steady flow. Ocean Eng 2015;110:51–61. http://dx.doi.org/10.1016/j.oceaneng.2015.09.052.
[44] Nishino T, Willden R. Effects of 3-D channel blockage and turbulent wake mixing on the limit of power extraction by tidal turbines. Int J Heat Fluid Flow 2012;37:123–35. http://dx.doi.org/10.1016/j.ijheatfluidflow.2012.05.002.
[45] Schluntz J, Willden R. The effect of blockage on tidal turbine rotor design and performance. Renew Energy 2015;81:432–41. http://dx.doi.org/10.1016/j.renene.2015.02.050.
[46] Kolekar N, Banerjee A. Performance characterization and placement of a marine hydrokinetic turbine in a tidal channel under boundary proximity and blockage effects. Appl Energy 2015;148:121–33. http://dx.doi.org/10.1016/j.apenergy.2015.03.052.
[47] Bahaj A, Molland A, Chaplin J, Batten W. Power and thrust measurements of marine current turbines under various hydrodynamic flow conditions in a cavitation tunnel and a towing tank. Renew Energy 2007;32:407–26. http://dx.doi.org/10.1016/j.renene.2006.01.012.
[48] Whelan J, Graham J, Peiro J. A free-surface and blockage correction for tidal turbines. J Fluid Mech 2009;624:281–91. http://dx.doi.org/10.1017/S0022112009005916.
[49] Churchfield MJ, Li Y, Moriarty PJ. A large-eddy simulation study of wake propagation and power production in an array of tidal-current turbines. Phil Trans Royal Soc Math Phys Eng Sci 2013;2013:371. http://dx.doi.org/10.1098/rsta.2012.0421.
[50] Thomson J, Polagye B, Durgesh V, Richmond M. Measurements of turbulence at two tidal energy sites in Puget Sound, WA. IEEE J Oceanic Eng 2012;37:363–74. http://dx.doi.org/10.1109/JOE.2012.2191656.